Analysis on the Floquet Scattering Lobes from Microwave Calibration Targets

Qingsong Gao[1], Yuan Tao[1], Chunyan Jing[1], Ming Jin[2, *], Dong Xia[3], and Ming Bai[3]

Abstract—The calibration target is a vital instrument for calibrating space-borne microwave radiometers, and its emissivity performance must be accurately determined before usage. Based on the Kirchhoff's law of thermal equilibrium, the emissivity of a calibration target can be determined from its electromagnetic reflectivity, which is defined as space integration of scattering. However, due to the general shape of periodic coated sharp pyramids, the scattering from calibration targets shows Floquet mode properties with scattering lobes in upper space. That phenomenon must be considered in the reflectivity measurement of calibration target, especially in the mono-static backscattering configuration. To support such backscattering-based reflectivity measurement, the Floquet mode and scattering patterns from periodic unit and finite-sized array are investigated by numerical simulations, more specifically, by the finite-difference time domain (FDTD) algorithm. The investigations include the scattering power distributions among scattering lobes from coated and bare pyramid arrays, and the ratio of total reflection to backscattering in cases of typical parameters. It is found in the millimeter wave region that the scattering power from bare pyramids is still concentrated in the backscattering lobe in the mono-static configuration, while for the coated pyramids the scattering power is distributed around Floquet modes. For the considered geometry and coating parameters, the power ratio of total scattering to backscattering can be more than 10 dB at the cared frequencies. After all, the numerical results provide referencing correction factor for actual measurement studies. It is also validated by numerical results and suggested in practice, to use periodic simulations of low computational burden to evaluate the compensation factor for the mono-static reflectivity measurement.

1. INTRODUCTION

The microwave calibration target is a vital instrument mounted on satellite to calibrate the space-borne radiometers, by providing referencing brightness temperature radiation [1–3]. For such a purpose, the calibration target is required to have a high emissivity and low surface temperature gradient [3–5]. Based on the Kirchhoff's law of thermal equilibrium, the emissivity of a target sums its reflectivity equal to 1, which means that achieving a high emissivity is equivalent to realizing a low reflectivity. As a consequence, the calibration target is generally designed in shape of periodic array of coated sharp metal pyramids/cones, for low reflection in the microwave band [4, 5]. Actually, one of the most important challenges in improving the accuracy of microwave radiometry is raising the precision of this referencing source. For this goal, long term researches have been conducted, ranging from target designs [5, 7], numerical simulations [5–13], measurement studies [3, 14–16], to recent brightness radiation modeling [16–18].

---

* Corresponding author: Ming Jin (jinmingaps@163.com).
[1] Science and Technology on Vacuum Technology and Physics Laboratory, Lanzhou Institute of Physics, Lanzhou 730000, P. R. China.
[2] State Key Laboratory of Remote Sensing Science, Institute of Remote Sensing and Digital Earth, CAS, Beijing 100090, P. R. China.
[3] School of Electronic Information Engineering, Beihang University, Beijing 100191, P. R. China.

Since the calibration target is the referencing source for quantitative radiometer observations, its emissivity performance must be measured and determined before functioning on board [2, 3, 14–16]. Actually in practice, the emissivity performance of the calibration target is determined by founding its electromagnetic reflectivity, which is done by the scattering measurements [14–16]. By now, the required emissivity of calibration target has been risen to $0.999\times$ for space-borne radiometer missions. It means that a reflectivity less than -30 dB has to be measured and examined correctly. Generally, there are two issues in the reflectivity measurement of a calibration target: First, a low overall reflectivity leads to the scattering very weak to be accurately captured; Second, the reflectivity is defined by the integration of scattering within the upper-space, while for the scattering measurement it is almost impossible to cover the whole region to fulfill the integration. After all, the reflectivity has to be inferred based on measured weak scattering at/in limited space positions/regions.

In fact, the first issue can be tackled by the space standing-wave methods, which is developed for extracting weak backscattering signal in the mono-statistic measurements [14–16]. The second issue, however, is yet to be addressed. Due to the periodic structure of the calibration target, its scattering is constructed by scattering lobes in the upper-space, namely, Floquet modes [6–8, 10]. In the mono-static scattering measurement, the reflectivity has to be extracted from the measured back-scattering, and a correction factor is required in this case. This correction factor is hard to predict by analytical models such as those for very rough surfaces, due to the periodic and artificial nature of the calibration target. In this work, simulations based on full-wave numerical method are conducted to obtain the scattering distributions from the calibration target, for this specific need in the mono-static measurement. The relationship between back-scattering and total reflectivity is to be investigated, especially at high frequency such as 89 GHz where a large number of Floquet lobes exist. The basic structure of coated sharp pyramids is considered in this paper, while scattering from the bare pyramids with the same geometric parameters is also addressed in comparisons.

The rest of this paper consists of 3 parts. In Section 2, the theoretic relationship between scattering and reflectivity of calibration targets is concluded, leading to the purpose and configurations of the simulation studies conducted in this paper. Then in Section 3, the numerical results are given and discussed, in the mono-static measurement configuration. Finally, conclusions are drawn in Section 4.

2. SCATTERING AND REFLECTIVITY FROM CALIBRATION TARGETS

One of the hardest tasks in the mono-static measurement for the reflectivity of calibration targets is estimating the overall reflectivity based on measured backscattering, at the presence of Floquet scattering lobes due to the periodic structure nature. In this section, we review the linkage between scattering lobes and reflectivity, and the procedures of the mono-static measurements. Then the simulation configurations are demonstrated, for extracting and concluding the quantitative relationship between the backscattering and total reflectivity.

2.1. Emissivity, Reflectivity and Scattering

Based on the Kirchhoff's law of thermal equilibrium, the radiating ability of a target is the same as its absorption, therefore, emissivity $e = \alpha = 1 - r$. Specifically, the emissivity of the calibration target at frequency f of polarization h or v toward the direction of (θ_i, ϕ_i) can be determined by the electromagnetic reflectivity to illumination from (θ_i, ϕ_i) of h or v, as in Eq. (1). In this paper, we only consider the emissivity towards normal direction ($\theta_i = 0°$ and $\phi_i = 0°$), as most calibration targets are applied to provide reference bright temperature radiation at this direction. In this case, $e^h = e^v$, due to the structural symmetry of calibration targets. For the ease of demonstration, θ_i, ϕ_i and polarization h or v will be omitted in the rest of this paper.

$$e^h(f, \theta_i, \phi_i) = 1 - r^h(f, \theta_i, \phi_i), \quad e^v(f, \theta_i, \phi_i) = 1 - r^v(f, \theta_i, \phi_i) \tag{1}$$

In Figure 1, the configuration of reflectivity determination of the calibration target is shown. The structure considered in this work is periodic coated sharp pyramids, and important geometry parameters include: uniform coating thickness t, period p, height (h) to period (p) ratio which can also be described by the vertex angle β. The reflectivity is defined by the ratio of integrated scattered power to the
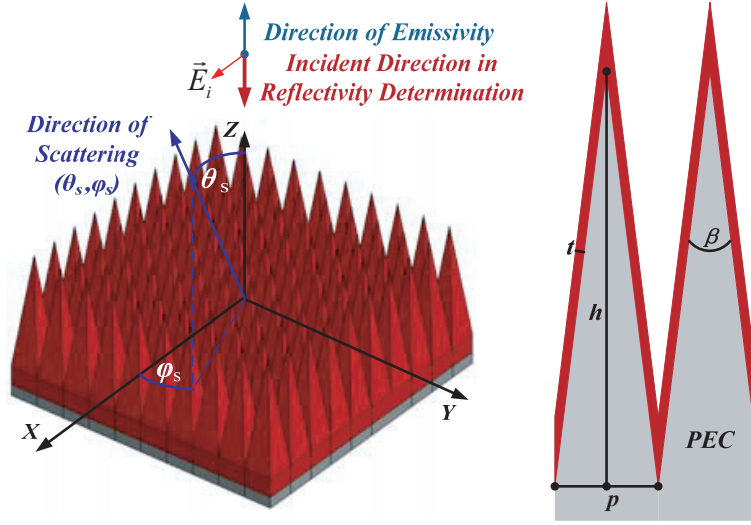
Figure 1. Configuration of scattering from microwave calibration targets consisting of periodic coated sharp pyramids.

intercepted illumination power. The total reflection can be obtained by either integrating far-field differential scattering coefficients in half space (Eq. (2), [6, 9, 10]) or at any close aperture around the targets (Eq. (3)). In both ways, it requires full scattering field distributions to fulfill the integration. However, in practical measurements, this requirement seems too difficult to be met.

$$r(f) = \frac{1}{4\pi} \iint_{2\pi} \gamma(f, \theta_s, \phi_s) \sin\theta_s d\theta_s d\phi_s$$
$$\gamma(f, \theta_s, \phi_s) = \frac{S(f, \theta_s, \phi_s)4\pi}{P_{inc}(f)} \tag{2}$$

where $S(f\theta_s\phi_s)$ stands for the angular scattering power density towards $(\theta_s\phi_s)$ in far field, while $\gamma(f\theta_s\phi_s)$ stands for the differential scattering coefficients, the integration of which over space leads to the reflectivity, and P_{inc} is the intercepted illumination power by the calibration target.

$$r(f) = \frac{P_{refl}(f)}{P_{inc}(f)} = \frac{\frac{1}{2} \iint_{\Sigma} \text{Re}\left(\vec{E}_s \times \vec{H}_s^* \cdot \hat{n}\right) dS}{P_{inc}(f)} \tag{3}$$

where Σ stands for any aperture that covers the scattered power around the calibration target in the near-field region, and P_{refl} is the overall reflected/scattered power by the calibration target.

The periodic structure of the calibration target will exhibit Floquet mode scattering properties. Due to the coherent summation of scattering from each periodic unit, there will be directions where scattering from each units are additive, also directions where scatterings cancel with each other. Considering a normal illumination with a plane-wave like phase distribution, there will be at least one additive scattering lobe at the mirrored direction in all frequency region which is the basic Floquet mode or the backscattering lobe, and more scattering lobes will rise when the frequency is high enough so that $c/f = \lambda < p$ [6–8, 10]. The angular positions of those scattering lobes can be found based on the Floquet mode theory as in Eq. (4), apparently only limited pairs of (m, n) can lead to actual scattering lobes (Satisfying $k_x^2 + k_y^2 < k^2$) [6]. The existence of scattering lobes means that the scattering power will be distributed in those lobes. As a consequence, the scattering power may not be concentrated in the backscattering lobe.

$$\begin{pmatrix} \sin\theta_s^{m,n}\cos\phi_s^{m,n} \\ \sin\theta_s^{m,n}\sin\phi_s^{m,n} \\ \cos\theta_s^{m,n} \end{pmatrix} = \begin{pmatrix} k_x^m/k_0 \\ k_y^n/k_0 \\ k_z^{m,n}/k_0 \end{pmatrix} = \begin{pmatrix} m\cdot\lambda/p \\ n\cdot\lambda/p \\ \sqrt{1 - (m^2+n^2)\cdot(\lambda/p)^2} \end{pmatrix}, \quad m, n = -\infty\ldots0\ldots1\ldots\infty \tag{4}$$

Here, k_x, k_y, k_z are the wave numbers towards the X, Y, and Z directions, respectively. And ($\theta_s^{m,n}$, $\phi_s^{m,n}$) is the propagation direction of the (m, n) order Floquet lobe in the spherical coordinate system.

2.2. Reflectivity Determination Based on Mono-Static Scattering Measurements

In Figure 2, the reflectivity determination in the mono-static scattering measurement is sketched [14–16]. In most cases, the incident illumination is at the normal direction (θ_i, $\phi_i = 0°$) to capture the mirrored reflection (backscattering). The key idea of this setup is that by implementing a variable distance D between the T/R antenna and the calibration target, one can distinguish the fixed reflection within antenna (S_{ant}) and the weak backscattering signal (S_{ct}). Using the measured S-parameter from referencing flat metal plate (S_{pl}), the measured backscattering can be calibrated into backscattering voltage reflectivity Γ_{ct} of the calibration target [14], as in Eq. (5). Then by estimating a correction factor C_g counting for the ratio of total scattering power to the backscattering power, the reflectivity r can be inferred as in Eq. (6):

$$|S_{pl}| = |C_p| \cdot |\Gamma_{pl}| \quad |\Gamma_{pl}| = 1 \quad |S_{ct}| = |C_p| \cdot |\Gamma_{ct}|$$
$$\Rightarrow |\Gamma_{ct}| = |S_{ct}| / |S_{pl}| \tag{5}$$

where C_p is the correction factor for the wave propagation attenuation between the antenna and the target, and it is assumed that by placing the reference metal plate at an appropriate position, C_p remains the same in the two times of measurements. Large aperture antennas with plane-wave like phase-front are more favorable in this configuration, for better gathering scattering power and reducing clutters from background (better focusing). This is also the case to be simulated and analyzed in this work. A lens antenna or quasi-optical (QO) reflector can be used to provide the required plane-wave like (considering phase only) illumination and receiving aperture (Figure 2), in the low frequency (up to Ka band) and high frequency region, respectively.

$$r = |\Gamma_{ct}|^2 \cdot C_g \tag{6}$$

After all, it is assumed that the backscattering from the calibration targets can be actually and steadily measured, and the focus of our work is to discuss the relationship between the backscattering and the overall reflectivity of the target, quantitatively counted by C_g.

The difficulties in inferring C_g are because of the periodic structure of the calibration target. When the frequency is high so that p is larger than λ, Floquet modes are excited, and estimations based on very rough surface theories are not sufficient to include this fact. Then, scattering power may be scattered into a number of scattering lobes, other than only in the mirroring scattering lobe (when only the basic Floquet mode exists). The Floquet theory can predict the angular positions of scattering lobes, but not
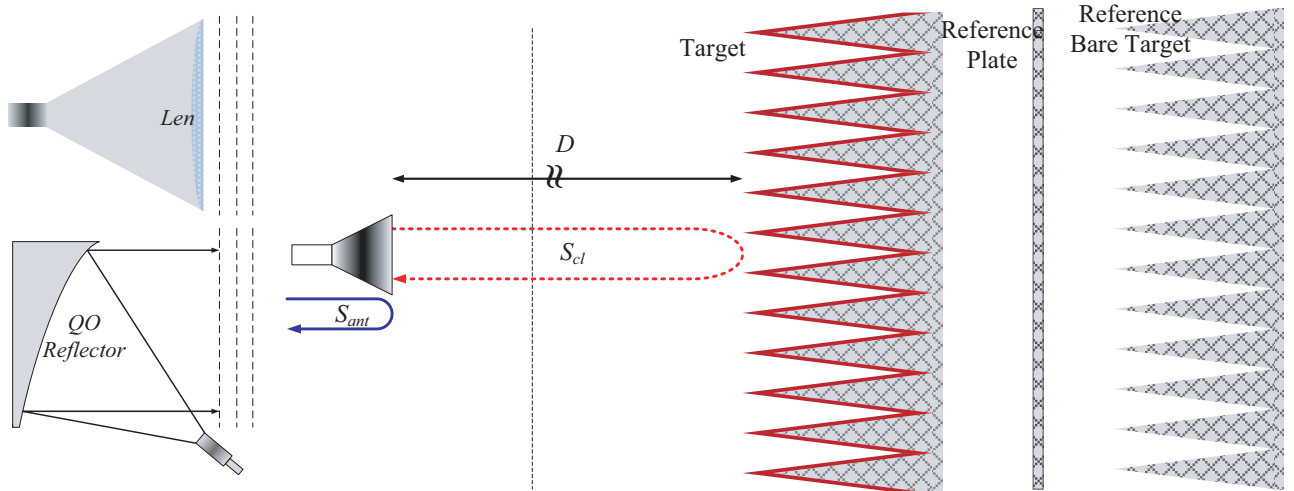
Figure 2. Configuration of mono-static reflectivity measurement for microwave calibration targets.

magnitude of each one. In this case, numerical simulations on the scattering from calibration targets become important source of information to predict C_g.

In this paper, we also consider the scattering from bare pyramids array without coating but with the same geometric parameters as the calibration target. The reasons in doing so include: 1, based on the bare pyramids array as reference, the assumption of equaling C_p in Eq. (5) is more stable, as bare pyramids are with almost the same total structural height as the calibration targets; 2, we want to investigate the possibility of canceling C_g in calibrating procedures by assuming that the scatterings from bare pyramids and coated pyramids share nearly the same power distribution properties among Floquet lobes. If this is correct or with acceptable error, then simple equation between measured backscattering from calibration target and referencing bare pyramids as in Eq. (7) can be used in determine the reflectivity.

$$r \approx |S_{ct}|^2 / |S_{bct}|^2 \qquad (7)$$

where S_{bct} is the measured backscattering voltage from bare target structure without the coating layer.

In this work, C_g from both the calibration targets and bare pyramids are to be investigated by numerical simulations based on the finite difference time domain (FDTD) method. And we focus on the high frequency region where a rich number of scattering lobes will be excited.

2.3. Numerical Solutions for Scattering from Calibration Targets

The FDTD is a time domain method based on discretizations of Maxwell equations in the differential form and is found to be one of the most suitable full-wave numerical solutions for modeling scattering from calibration targets [5–10]. It can be used in finding the scattering of incident beams from actual-sized targets just as in the mono-static measurement configuration [8–10] and can also be applied in finding wideband reflectivity of the coated structure based on a infinite-sized approximation with plane-wave illumination [6, 7, 13]. Figure 3 shows the two computation configurations. Apparently due to the presence of periodic boundary condition (PBC), the infinite-sized case requires much less computational resources, as only one single unit has to be meshed in the computation [4–6, 11]. In this work, we compare the Floquet scattering results by finite-sized and infinite-sized simulations, to discuss the possibility and reliability of the latter computation for providing correction information in the mono-static scattering measurement.
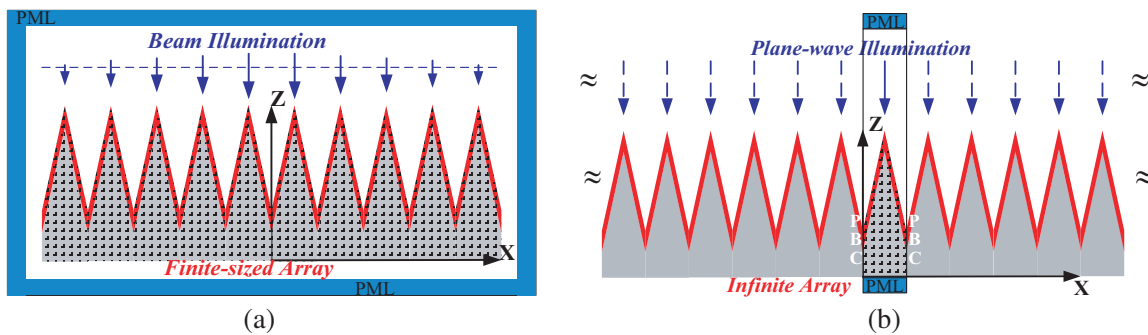
Figure 3. Configurations of numerical computation (FDTD) for scattering from microwave calibration targets: (a) finite-sized array case; (b) infinite-sized array case.

In both the above scattering computation configurations, there are recording apertures around the target to gather the scattered fields for further analysis. In the finite-sized computation configuration, the scattered fields around the target can be used to obtain the overall scattered power by surface integration, and the far-field scattering by the near-field to far-field transformation. Also, letting the illumination fields be the receiving antenna aperture fields (on the aperture denoted by A_above), one can also obtain the captured back-scattering power ($P_{backscatt}$) in the mono-static configuration, based on the aperture field correlation coefficients (C_i) as in Eq. (8). In the infinite-sized configuration, the scattered field due to the normal plane wave incidence can be expressed by a set of Floquet modes

as in Eq. (9), only those with a real k_z can carry scattering power off the structure and contributes to the total reflectivity [6, 7]. According to the Floquet theory, the total scattered power (P_{refl}) and backscattering power (the basic Floquet mode, $P_{backscatt}$), can be obtained by using Eqs. (10) and (11), respectively. In both cases, one can get the computed reflectivity r and C_g, the power ratio of the total scattering power to the backscattering.

In the finite-sized computation:

$$P_{backscatt} = \iint\limits_{A\_above} \text{Re}\left(\frac{\vec{E}_s \times \vec{H}_s^* \cdot \vec{n}_A}{2}\right) dS \cdot C_i^2$$

$$C_i = \frac{\left| \iint\limits_{A\_above} \vec{E}_s \cdot \vec{E}_i^* dS \right|}{\sqrt{\iint\limits_{A\_above} \vec{E}_i \cdot \vec{E}_i^* dS * \iint\limits_{A\_above} \vec{E}_s \cdot \vec{E}_s^* dS}} \tag{8}$$

In the infinite-sized computation:

$$\vec{E}_s = \sum_{m=-\infty}^{+\infty} \sum_{n=-\infty}^{+\infty} \vec{E}_s^{m,n} e^{-jk_x^m x - jk_y^n y - jk_z^{m,n} z}, \quad \vec{H}_s = \sum_{m=-\infty}^{+\infty} \sum_{n=-\infty}^{+\infty} \vec{H}_s^{m,n} e^{-jk_x^m x - jk_y^n y - jk_z^{m,n} z}$$

$$k_x^m = \frac{2\pi m}{p}, \quad k_y^n = \frac{2\pi n}{p} k_z^{m,n} = \sqrt[+]{k_0^2 - (k_x^m)^2 - (k_y^n)^2}, \quad k_0 = \frac{2\pi}{\lambda} \tag{9}$$

$$P_{refl} = \sum_m \sum_n \iint\limits_{Ap} \text{Re}\left(\frac{\vec{E}_s^{m,n} \times \vec{H}_s^{*m,n} \cdot \hat{k}^{m,n}}{2}\right) \cdot \frac{k_z^{m,n}}{k_0} dS \tag{10}$$

$$P_{backscat} = \iint\limits_{Ap} \text{Re}\left(\frac{\vec{E}_S^{0,0} \times \vec{H}_S^{*0,0} \cdot \hat{k}^{0,0}}{2}\right) dS = \iint\limits_{Ap} \text{Re}\left(\frac{\vec{E}_S^{ave} \times \vec{H}_S^{*ave} \cdot \hat{z}}{2}\right) dS \tag{11}$$

Here A_p stands for the aperture above the periodic structure, and E_s^{ave} is the space averaged E-field on the A_p.

And in both cases:

$$C_g = P_{refl}/P_{backscatt} \tag{12}$$

3. NUMERICAL RESULTS AND DISCUSSIONS

The numerical computations are based on the codes technically developed for the calibration target scattering, which have been well validated and applied in [6, 8, 10]. The coating materials considered in this work include MF112 and MF117 from ECCOSORB$^{\circledR}$ [19], which are frequently used on calibration targets [4–7, 13]. The relative permittivity (ε) and permeability (μ) of MF112 in wideband can be

Table 1. Relative permittivity (ε) and permeability (μ) of the coating materials.

Frequency (GHz)	Material	$\varepsilon = \varepsilon' - \varepsilon'' i$	$\mu = u' - u'' i$
89	MF112	5.370-0.030i	0.645-0.163i
	MF117	19.989-0.159i	0.417-0.265i
54	MF112	5.375-0.049i	0.698-0.249i
	MF117	20.040-0.253i	0.397-0.475i
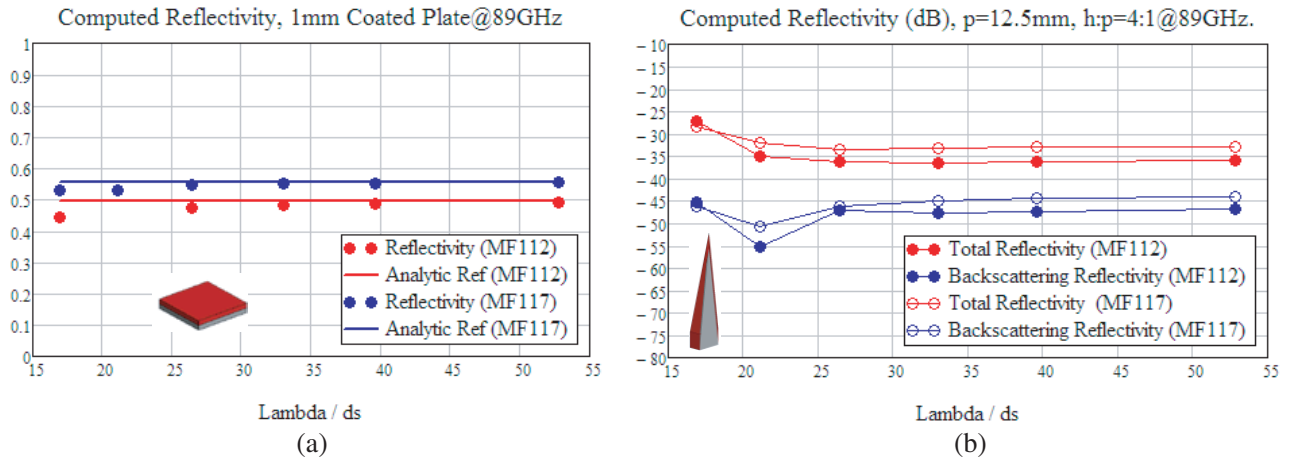
Figure 4. Convergence study for the discretized interval (ds) in FDTD computation (infinite-sized configuration), (a) comparison to analytical results for coated plate; (b) results for coated sharp pyramids.

modeled by the Debye dispersive model [7, 13]. Meanwhile, the MF117 can also be modeled as dispersive media. For reference, the relative permittivity and permeability of MF112 and MF117 used in this work are listed in Table 1 at cared frequencies. In Figure 4, results of convergence study upon the discretized interval (ds) used in FDTD are presented to validate the numerical solution. Also as can be observed, the discretized interval level of $1/40\lambda$ is necessary for accurately modeling the coating layer especially on the sharp geometry, which leads to $ds = 0.083333$ mm @89 GHz.

3.1. Wideband-Reflectivity Spectrum by Infinite-Sized Computations

Before analyzing the Floquet scattering from calibration targets, it is helpful and meaningful to review the typical wideband reflectivity performance of calibration targets. A typical h to p ratio of $4 : 1$ and a coating thickness of 1 mm on sharp pyramids are considered. The wideband reflectivity results by the infinite-sized simulations are shown in Figure 5, from 10 GHz to 100 GHz. The computation methods are from that in [7, 13], but the considerations of different coating materials and p are added. This frequency range covers practical working frequency points, such as 10.65 GHz, 18.7 GHz, 23.8 GHz, 36.5 GHz, 54 GHz, 89 GHz.

As can be observed, from 10 GHz to 20 GHz, the reflectivity of the calibration target decreases with increase of the frequency, and the reflectivity at 18.7 GHz is obviously lower than that at 10.65 GHz in all cases. As known from the previous studies [6–8], the reflectivity at the lowest frequency is the bottleneck of the design, as it yields the lowest emissivity in most cases. Then the frequency region from 15 GHz to 60 GHz seems a safe area in the case of MF112 coating, where a reflectivity level of −40 dB can be easily achieved. Those reflectivity peaks due to the excitation of the first and second order Floquet modes can be avoided at cared frequency by adjusting the period p. However, these results show that the high frequency region should also be noted when a thin coating (1 mm) of MF112 is applied. For example, at 89 GHz the reflectivity is above −40 dB with $p = 12.5$ mm. The results of MF117 coating are also included in analysis, which yields good low-frequency results but not so good high frequency performance. In those figures, the reflectivity results only due to the backscattering (basic or zero-order Floquet mode) are also plotted. It is clear that the backscattering reflectivity varies smoothly with the frequency. After high-order Floquet modes are excited, the total reflectivity is obviously higher than the backscattering reflectivity.

Then, the scattering from the bare pyramids array is considered. The results by infinite-sized computation are presented in Figure 6, considering different period sizes and h to p ratios. It is interesting that,for the h to p ratio of $4 : 1$, the backscattering contributes most of the total reflectivity. This is very different from the results in Figure 5, where the backscattering reflectivity is much lower than the total reflectivity. It can also be observed that the lower height or sharpness leads to a weaker
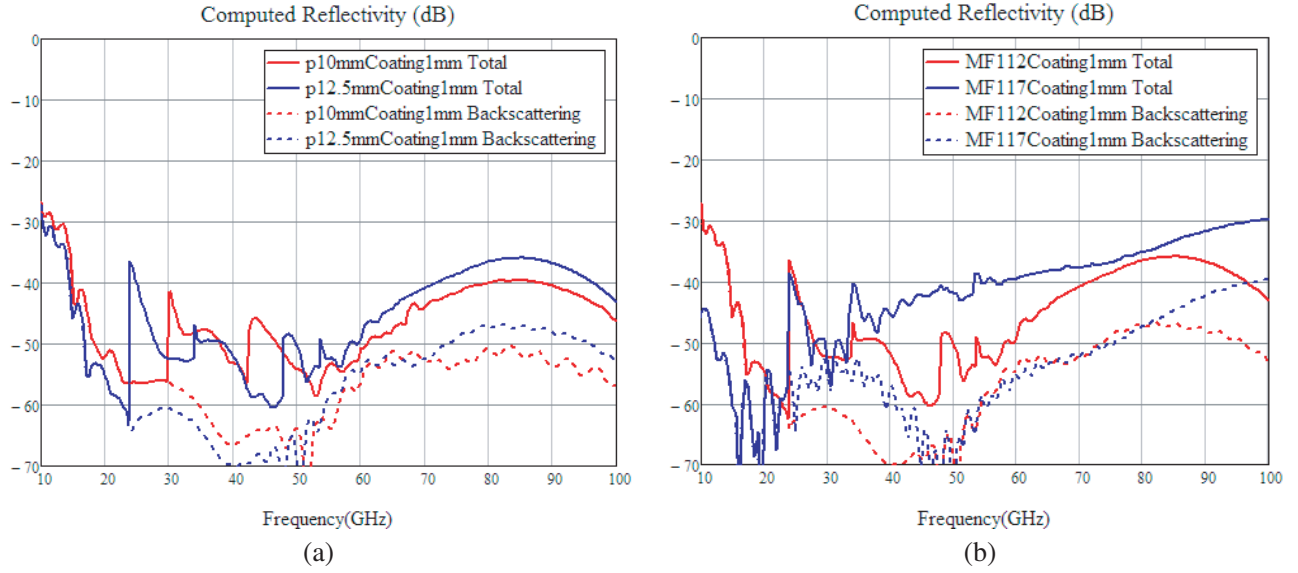
Figure 5. Wide-band reflectivity of microwave calibration target designs by infinite-sized computation, comparisons between different period size and different coating materials. (a) Considering MF112 coating on $4:1$ pyramids; (b) considering $1\,\text{mm}$ coating on $4:1$ pyramids, $p = 12.5\,\text{mm}$.
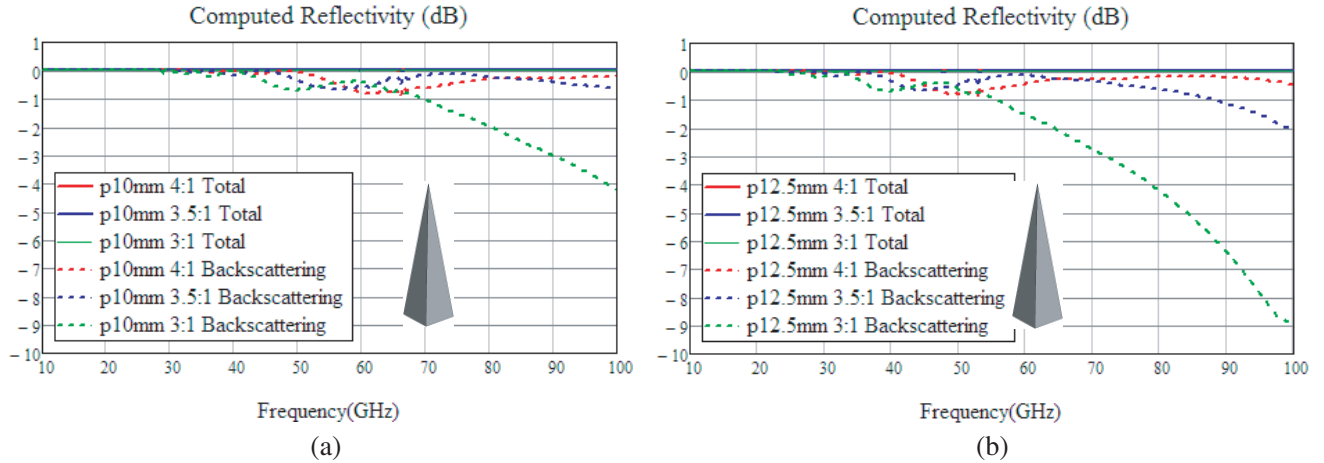
Figure 6. Wide-band reflectivity of bare pyramids by infinite-sized computation, comparisons between different h to p ratios in cases different period size. (a) $p = 10.0\,\text{mm}$; (b) $p = 12.5\,\text{mm}$.

backscattering for the bare pyramids. It means that the scattered power distribution among Floquet modes can be directly altered by the geometry of each unit. It should also be noted that for the naked PEC pyramids array, the total reflectivity should be 1 at the whole frequency region no matter how many Floquet modes are excited, as the total reflectivity results plotted in Figure 6. In this case, when higher order Floquet modes are excited, an amount of scattering power will be redistributed into those lobes from the backscattering. This is different from the case of absorptive coating, where the excitation of high order Floquet modes leads to a increase of total reflectivity, in other words, leads to the birth of new reflectivity contributions, especially for the first/second order Floquet modes. By now from the results it is clear that although the bare pyramids array can share the same geometry parameters as the calibration target (with coating), the reflectivity power distributing properties among Floquet modes are very different. In other words, C_g of the two targets are with a nonnegligible difference, hence Eq. (7) is not suggested in practical usage for the calibration targets of sharp pyramids.

As should be noted, the results presented above are from the infinite-sized computation where only

one period unit is actually meshed due to the PBC, in other words, in a very efficient and low-cost configuration. That computation configuration simulates a plane-wave illumination on a infinite-sized structure. Next, we will provide the results by finite-sized computation with a beam illumination as in the mono-static measurement configuration. Comparisons will also be made to validate the possibility of providing C_g by that low-cost infinite-sized computations.

3.2. Scattering Results from Finite-Sized Computations

In this section, the scattering results by finite-sized computations are presented, to discuss the scattering power distribution. The arrays of $12*12$ ($p = 10\,\mathrm{mm}$), and $10*10$ ($p = 12.5\,\mathrm{mm}$) are considered, with the illumination of Gaussian beam of the basic mode from the normal direction.
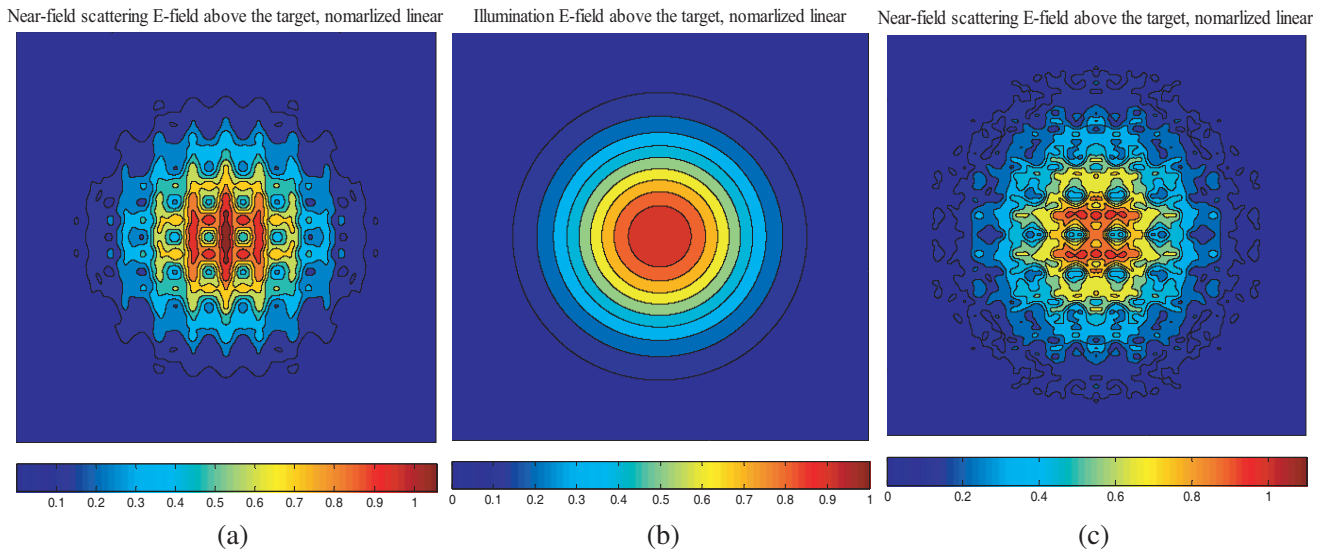
Figure 7. Computed near-field scattering fields distributions above the bare pyramids array and illumination beam, by finite-sized computation, normalized amplitude, at 89 GHz. (a) Scattering fields above the $12*12$ array, $p = 10\,\mathrm{mm}$; (b) illumination fields; (c) scattering fields above $10*10$ array, $p = 12.5\,\mathrm{mm}$.
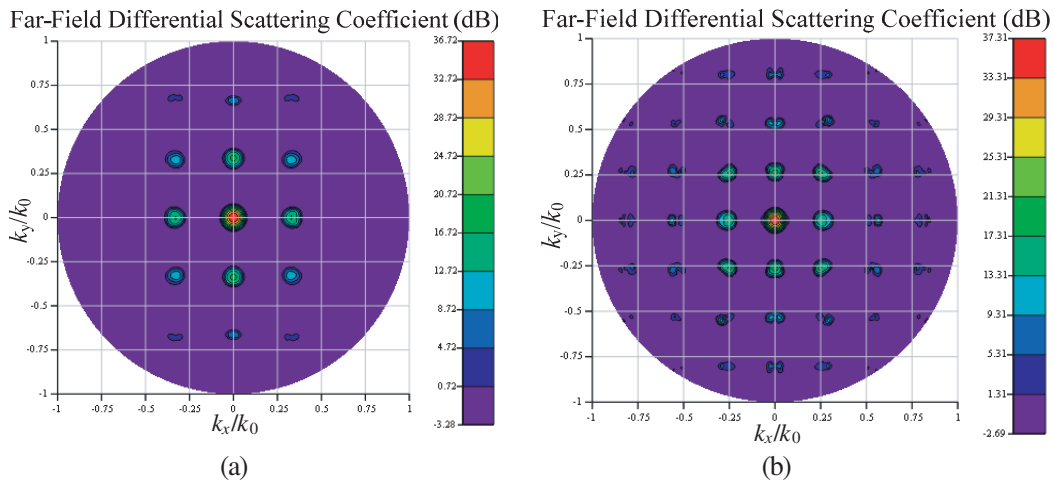
Figure 8. Computed far-field scattering distributions from the bare pyramids array, by finite-sized computation, in differential scattering coefficients at 89 GHz. (a) Scattering pattern in up-space, $12*12$ array, $p = 10\,\mathrm{mm}$; (b) scattering pattern in up-space, $10*10$ array, $p = 12.5\,\mathrm{mm}$.

In Figure 7, the computed scattering fields at 89 GHz above the bare-pyramids are plotted, with illumination field distribution as reference. The diffraction patterns due to Floquet scattering can be observed while the whole contour is still in a Gaussian form. In Figure 8, the far-field scattering lobes are presented in the $(k_x/k_0, k_y/k_0)$ manner for a clear view of the Floquet mode scattering. As can be observed, the backscattering lobe (at the center) is with the largest amplitude, and the amplitudes of other lobes are obvious lower.

In Figure 9, the computed scattering fields at 89 GHz above calibration targets (1 mm MF112 coating) are presented, with illumination field distribution as reference, strong diffraction patterns due to Floquet scattering can be well observed. In Figure 10, the far-field scattering lobes are also presented in the $(k_x/k_0, k_y/k_0)$ manner. Obviously, backscattering lobe (in the center) is no longer the major
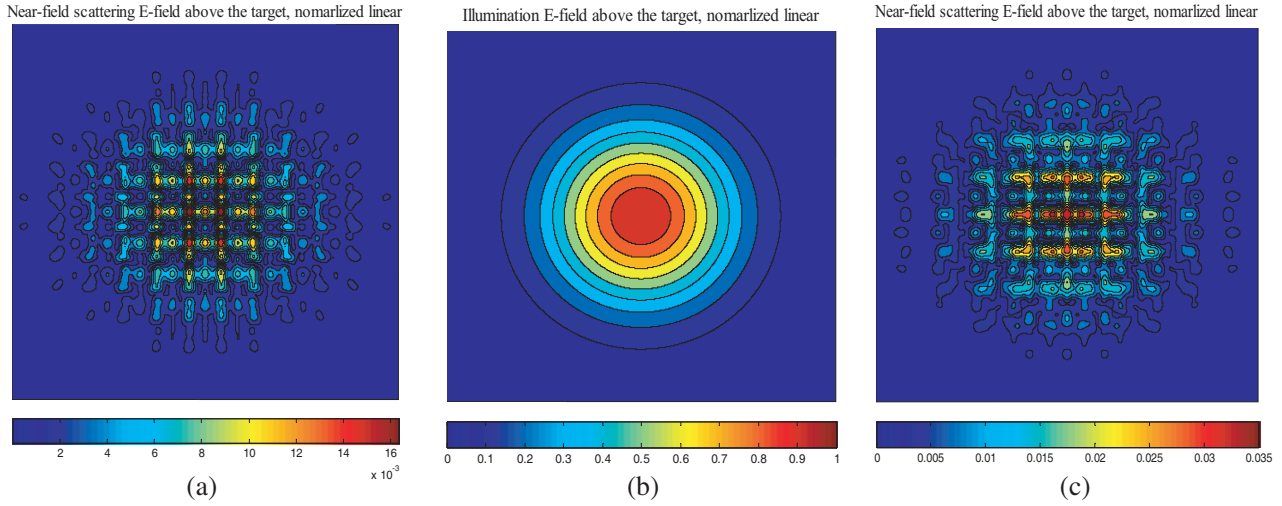
Figure 9. Computed near-field scattering field distributions above the calibration target and illumination beam, by finite-sized computation, normalized amplitude, at 89 GHz, height to period ratio $4:1$, 1 mm MF112 coating. (a) $12*12$ array, $p = 10$ mm; (b) illumination fields; (c) $10*10$ array, $p = 12.5$ mm.
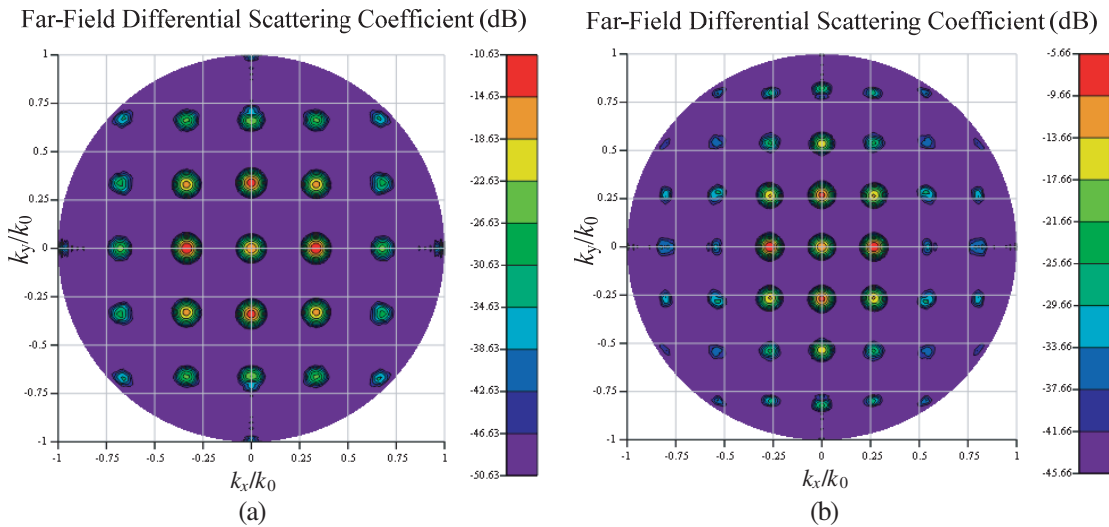
Figure 10. Computed far-field scattering distributions in up-space from the calibration target, by finite-sized computation, in differential scattering coefficients at 89 GHz, 1 mm MF112 coating, h to p ratio: $4:1$. (a) $p = 10$ mm, $12*12$ array; (b) $p = 12.5$ mm, $10*10$ array.
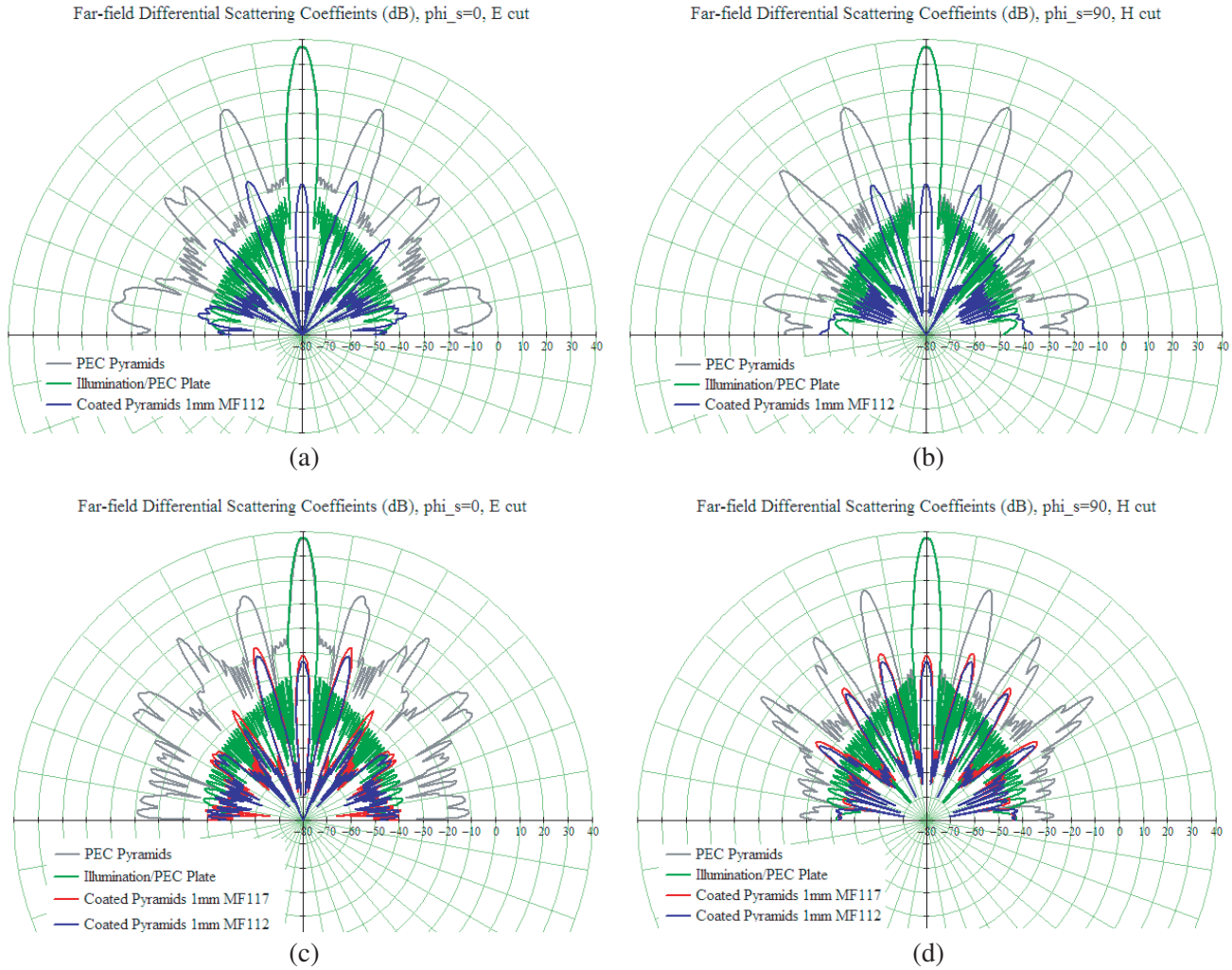
Figure 11. Computed far-field scattering distributions in up-space from the calibration target and bare pyramids, by finite-sized computation, in differential scattering coefficients at 89 GHz, h to p ratio 4 : 1. (a) $p = 10$ mm, $12 * 12$ array, E-cut; (b) $p = 10$ mm, $12 * 12$ array, H-cut; (c) $p = 12.5$ mm, $10 * 10$ array, E-cut; (d) $p = 12.5$ mm, $10 * 10$ array, H-cut.

contribution to the total reflectivity, and the amplitudes of other lobes are obviously larger. In Figure 11, the Far-field scattering patterns of PEC pyramids, 1 mm MF112 and 1 mm MF117 coated pyramids are compared in the E and H cut planes at 89 GHz. The difference in the scattering power distributions among scattering lobes can be clearly observed for the bare pyramids and coated pyramids. For the PEC pyramids, the scattering power is concentrated in the backscattering lobe, while for the absorptive coated pyramids, scattering power is more distributed in numbers of scattering lobes. Then the C_g computed in the infinite and finite sized configurations can be compared in each set of parameters, as listed in Table 2. Clearly, the ratio factors C_g by the infinite-sized and finite-sized computations come to an agreement. Also it can be found that, at 89 GHz and with the considered parameters, the reflectivity ranges from -40 dB to -30 dB, and the computed C_g are all above 11 dB.

3.3. Discussions on C_g for Absorptive Coated Pyramids

The C_g variation properties of the coated pyramids are important information useful to the actual reflectivity measurements. In this section, more samples are considered to discuss the C_g variation.

First, the total reflectivity and backscattering reflectivity are presented and analyzed at 89 GHz

Table 2. Comparison of computed reflectivity and C_g at 89 GHz.

Parameters	Infinite-sized computation			Finite-sized computation		
$h : p = 4 : 1$, @89 GHz	r_{total}	r_{back}	$\mathbf{C_g}$	r_{total}	r_{back}	$\mathbf{C_g}$
PEC, $p = 10.0$ mm	0.0 dB	−0.3 dB	**0.3 dB**	0.0 dB	−0.5 dB	**0.5 dB**
PEC, $p = 12.5$ mm	0.0 dB	−0.2 dB	**0.2 dB**	0.0 dB	−0.8 dB	**0.8 dB**
1 mm MF112 $p = 10.0$ mm	−40.2 dB	−52.5 dB	**12.3 dB**	−39.9 dB	−52.2 dB	**12.3 dB**
1 mm MF112 $p = 12.5$ mm	−36.5 dB	−47.7 dB	**11.2 dB**	−36.4 dB	−47.9 dB	**11.5 dB**
1 mm MF117 $p = 12.5$ mm	−33.0 dB	−44.5 dB	**11.5 dB**	−32.9 dB	−44.3 dB	**11.4 dB**

Table 3. Comparison of computed reflectivity and $\mathbf{C_g}$ at 54 GHz.

Parameters	Infinite-sized computation			Finite-sized computation		
$h : p = 4 : 1$, @54 GHz	r_{total}	r_{back}	$\mathbf{C_g}$	r_{total}	r_{back}	$\mathbf{C_g}$
PEC, $p = 12.5$ mm	0.0 dB	−0.7 dB	**0.7 dB**	0.0 dB	−0.8 dB	**0.8 dB**
1 mm MF112 $p = 12.5$ mm	−50.3 dB	−62.4 dB	**12.2 dB**	−50.8 dB	−64.3 dB	**13.5 dB**
1 mm MF117 $p = 12.5$ mm	−38.9 dB	−59.7dB	**20.8 dB**	−41.3 dB	−61.4 dB	**20.1 dB**
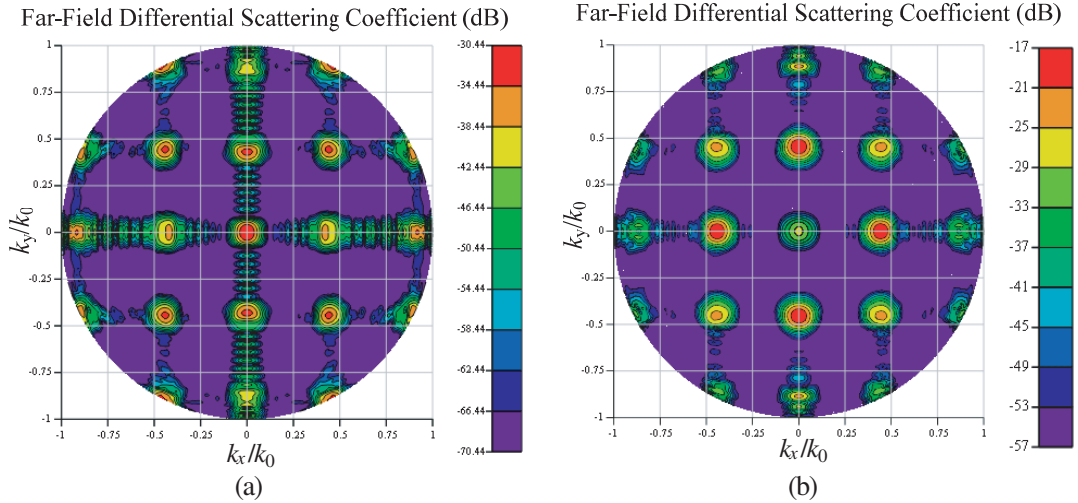
Figure 12. Computed far-field scattering distributions in up-space from the calibration target, by finite-sized computation, in differential scattering coefficients at 54 GHz, $p = 12.5$ mm, $10 * 10$ array, h to p ratio: $4 : 1$, (a) 1 mm MF112 coating; (b) 1 mm MF117 coating.

for the 1 mm coating, where the backscattering is above −50 dB, and the computed C_g is above 11 dB. Then, it is interesting to check the reflectivity at 54 GHz for the 1 mm MF112 and MF117 coatings, where the backscattering is very weak as predicted in Figure 5(b). As can be observed at 54 GHz, the backscattering reflectivity results with 1 mm coating are around −60 dB, while the total reflectivity can be about −40 dB with MF117 coating, but less than −50 dB with MF112 coating. Those results can also be supported by the finite-sized computed scattering presented in Figure 12 and Table 3: the computed C_g is 12 dB $\sim$ 13 dB for the MF112 coating and about 20 dB for the MF117 coating. From the far-field scattering results presented in Figure 13, it is clear that the first-order Floquet lobes are with strong amplitudes contributing to the large C_g in the case of MF117 coating. This example shows that different coatings may lead to different C_g, even the backscattering levels are close. C_g

Far-field Differential Scattering Coefficients (dB), phi_s=0, E cut

Far-field Differential Scattering Coeffieints (dB), phi_s=90, H cut

(a)

(b)
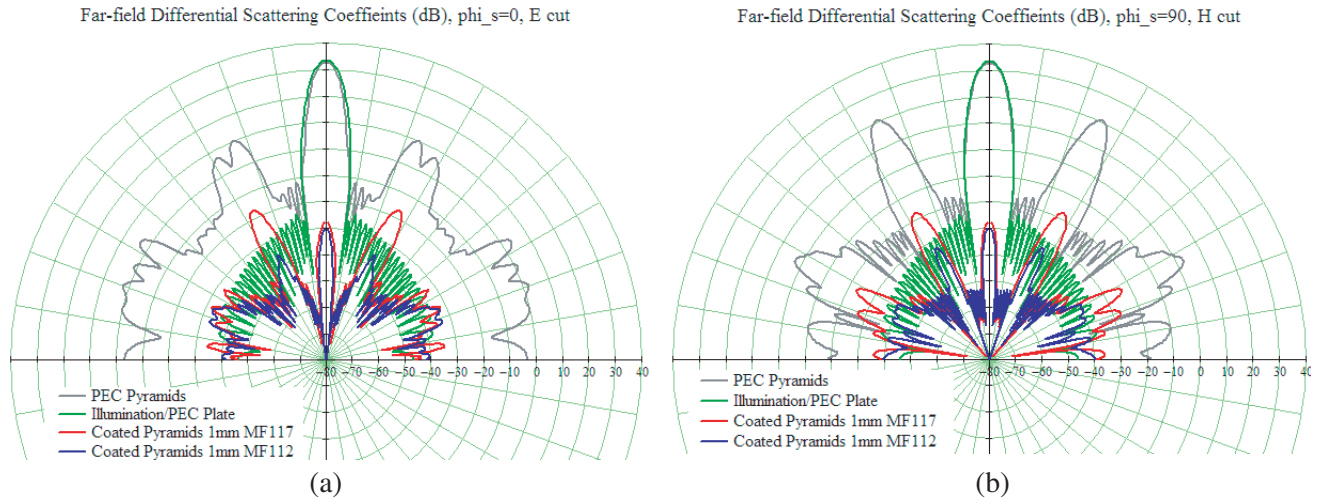
Figure 13. Computed far-field scattering distributions in up-space from the calibration target and bare pyramids, by finite-sized computation, in differential scattering coefficients at 54 GHz, h to p ratio $4:1$. (a) $p = 12.5$ mm, $10 * 10$ array, E-cut; (b) $p = 12.5$ mm, $10 * 10$ array, H-cut.

Computed Reflectivity (dB), p = 12.5mm, h:p = 4:1.

Computed Reflectivity (dB), p = 12.5mm, h:p = 4:1.

Coating Thickness(mm)

Coating Thickness(mm)

(a)

(b)
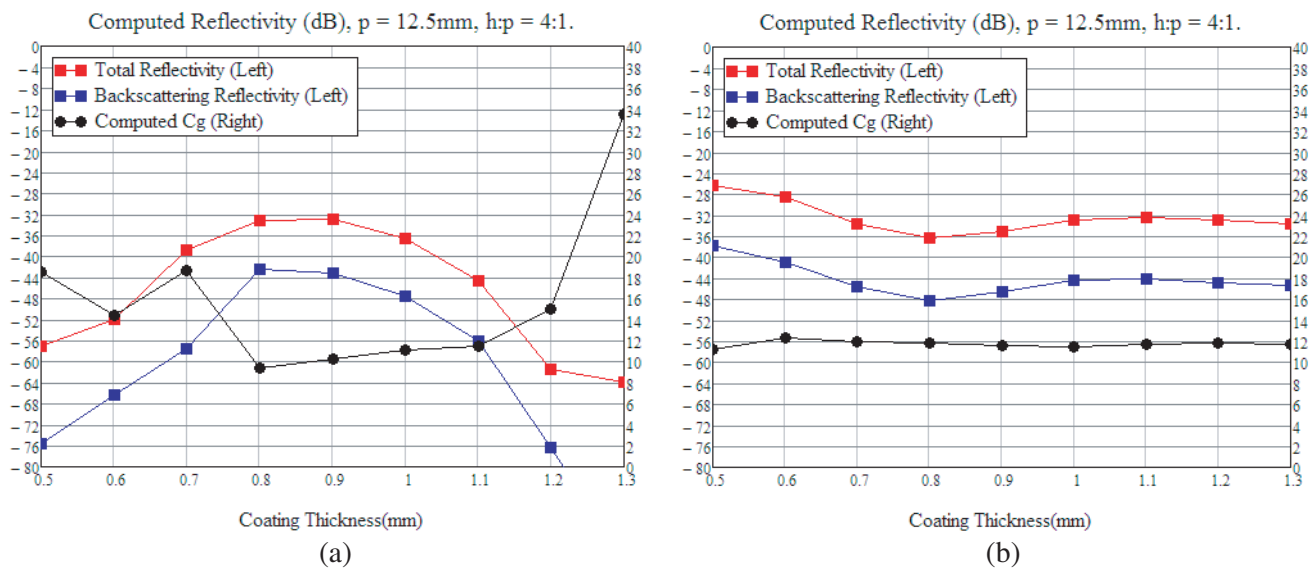
Figure 14. Computed total and backscattering reflectivity versus coating thickness, by infinite-sized computation at 89 GHz, $p = 12.5$ mm, h to p ratio $4:1$. (a) MF112 coating; (b) MF117 coating.

may become hardly predictable when the backscattering is very weak. Therefore, it is advised to use numerical simulations to estimate or check C_g based on actual geometry/coating parameters, even when the backscattering is indeed weak.

Then, back to 89 GHz, we check the variation of C_g of the coating pyramids, with the coating thickness. p is 12.5 mm, and MF112 and MF117 are considered. The sweeping of coating thickness t ranges from 0.5 mm to 1.3 mm, and the results by infinite-sized simulations are plotted in Figure 14. As can be seen, when the backscattering is above -50 dB, C_g is about $10 \sim 13$ dB, and a trend of higher C_g in the case of lower backscattering can be concluded. These results also show that when the reflectivity is very weak, C_g becomes hardly predictable. Fortunately, 89 GHz is in the high not the middle frequency region, where backscattering is not at the bottom, and also the excitation of high-order Floquet modes will not lead to obvious perturbation of total scattering as the 1st–3rd order modes do (Figure 5). In

this case, a prediction of C_g about $10 \sim 13$ dB should be sufficient for the backscattering above -50 dB, corresponding to the total reflectivity larger than -40 dB and the emissivity determination of $0.9999+$.

4. CONCLUSION AND PERSPECTIVES

In this work, mono-static reflectivity measurement for calibration targets is reviewed and discussed, then numerical simulations are performed to obtain the scattering power distribution properties among Floquet scattering lobes. Both low-cost infinite-sized and more exact finite-sized computations are done to obtain the information, or specifically, the C_g defined by the ratio of the total reflection to backscattering. The results by those computations show that: 1, although the same geometry parameters can be shared, C_g of the bare sharp metal pyramids is quite different from that of the absorptive coated pyramids; 2, a coarse trend that lower backscattering leads to a larger C_g can be concluded for the sharp coated pyramids, and C_g becomes highly unpredictable when the backscattering is indeed weak; 3, at a high frequency such as 89 GHz (W band) and for the backscattering above -50 dB, the computed C_g is about 10 dB $\sim$ 13 dB for the absorptive coated sharp pyramids with considered geometry parameters. Those findings are useful and meaningful for the accurate emissivity determination of actual calibration targets, which in turn contributes to the precision improvement of passive microwave remote sensing. Future works will be further concluding quantitative trends and investigating calibration targets consisting of coated cones.

ACKNOWLEDGMENT

REFERENCES

1. Yang, H., F. Weng, L. Lv, N. Lu, G. Liu, M. Bai, Q. Qian, J. He, and H. Xu, "The FengYun-3 microwave radiation imager on-orbit verification," *IEEE Trans. Geosci. Remote Sens.*, Vol. 49, No. 11, 4452–4560, 2011.

2. Wang, Z.-Z., J. Li, S. Zhang, and Y. Li, "Prelaunch calibration of microwave humidity sounder on China's FY-3A," *IEEE Geosci. Remote Sens. Lett.*, Vol. 8, No. 1, 29–33, 2011.

3. Nian, F., Y.-J. Yang, Y.-M. Chen, D.-Z. Xu, and W. Wang, "Recent progress on space-borne microwave sounder pre-launch calibration technologies in China," *Journal System Engineering Electronics*, Vol. 19, No. 4, 643–650, 2008.

4. Randa, J., A. Cox, and D. K. Walker, "Proposed development of a national standard of microwave brightness temperature," *IEEE Proc. IGARSS*, 3979–3982, Jul. 31–Aug. 4, 2006.

5. Nian, F., Y.-J. Yang, and W. Wang, "Research of optimizing the microwave wide band blackbody calibration target," *Journal of Systems Engineering and Electronics*, Vol. 20, No. 1, 6–12, 2009.

6. Wang, J.-H., J.-G. Miao, Y.-J. Yang, and Y.-M. Chen, "Scattering property and emissivity of a periodic pyramid array covered with absorbing material," *IEEE Trans. Antennas Propagat.*, Vol. 56, No. 8, 2656–2663, 2008.

7. Sandeep, S. and A. J. Gasiewski, "Electromagnetic analysis of radiometer calibration targets using dispersive 3D FDTD," *2012 IEEE Trans. Antennas Propagat.*, Vol. 60, No. 6, 2821–2828, 2012.

8. Jin, M., M. Bai, and J.-G. Miao, "Emissivity study of the array shaped blackbody in the microwave band," *Acta Phys. Sin.*, Vol. 61, No. 16, 164211, 2012 (in Chinese).

9. Wang, J.-H., Y.-J. Yang, J.-G. Miao, and Y.-M. Chen, "Emissivity calculation for a finite circular array of pyramidal absorbers based on Kirchhoff's law of thermal radiation," *2010 IEEE Trans. Antennas Propagat.*, Vol. 58, No. 4, 1173–1180, 2010.

10. Bai, M., M. Jin, N.-M. Ou, and J.-G. Miao, "On scattering from an array of absorptive material coated cones by the PWS approach," *2013 IEEE Trans. Antennas Propagat.*, Vol. 61, No. 6, 3216–3224, 2013.

11. Pan, G., M. Jin, L.-S. Zhang, M. Bai, and J.-G. Miao, "An efficient scattering algorithm for smooth and sharp surfaces: Coiflet-based scalar MFIE," *IEEE Trans. Antennas Propagat.*, Vol. 62, No. 8, 4241–4250, 2014.

12. Jin, M., M. Bai, L.-S. Zhang, G. Pan, and J.-G. Miao, "On the coiflet-TDS solution for scattering by sharp coated cones and its application to emissivity determination," *IEEE Trans. Geosci. Remote Sensing*, Vol. 54, No. 3, 1399–1409, 2016.

13. Sandeep, S. and A. J. Gasiewski, "Effect of geometry on the reflectivity spectrum of radiometer calibration targets," *IEEE Geosci. Remote. Sensing. Lett.*, Vol. 11, No. 1, 84–88, 2014.

14. Chen, C.-Y., F. Li, Y.-J. Yang, and Y.-M. Chen, "Emissivity measurement study on wide aperture microwave radiator," *IEEE Proc. ICMMT*, 914–917, Apr. 21–24, 2008.

15. Gu, D.-Z., D. Houtz, J. Randa, and D. K. Walker, "Reflectivity study of microwave blackbody target," *IEEE Trans. Geosci. Remote Sens.*, Vol. 49, No. 9, 3443–3451, 2011.

16. Houtz, D., D. K. Walker, and D.-Z. Gu, "Progress towards a NIST microwave brightness temperature standard for remote sensing," *IEEE Proc. IGARSS*, 3485–3488, Jul. 26–31, 2015.

17. Gu, D.-Z., J. Randa, and D. K. Walker, "A geometric error model for misaligned calibration target in passive microwave remote-sensing systems," *IEEE Geosci. Remote. Sensing. Lett.*, Vol. 10, No. 6, 1597–1601, 2013.

18. Gu, D.-Z. and D. K. Walker, "Application of coherence theory to modeling of blackbody radiation at close range," *IEEE Trans. Microwave Theory Tech.*, Vol. 63, No. 5, 1475–1488, 2015.

19. http://www.eccosorb.com/products-eccosorb-cr.htm; www.eccosorb.com/products-eccosorb-mf.htm.